ARTICLE

Check for updates

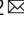# Design and evaluation of multi-core raspberry-like platinum nanoparticles for enhanced photothermal treatment

Erwann Guénin[1,8], Alexandre Fromain[2,8], Aida Serrano[3], Giacomo Gropplero[2], Yoann Lalatonne [4,5], Ana Espinosa[6,7] & Claire Wilhelm [2✉]

While gold-based nanoparticles are now commonly used in nanomedicine due to their stability and high plasmonic resonance, platinum nanoparticles are recently emerging as promising candidates for enhancing radiotherapy sensitivity due to their high atomic number. Here, we demonstrate that platinum-based nanomaterials with a multi-core structure also possess efficient near-infrared photothermal properties, despite platinum's maximum absorption being primarily in the ultraviolet region. The photothermal efficacy of these platinum multi-core raspberry-like nanoparticles is compared with single-core ultra-small platinum nanoseeds, within glioblastoma cancer spheroids, showcasing the potential of platinum nanocore aggregation for photothermal therapy in cancer treatment. Additionally, we used a microfabrication technique for high-throughput growth of spheroids in microwells to evaluate photothermal treatment on glioblastoma spheroids. Finally, X-ray absorption spectroscopy was conducted to analyze the stability and behavior of both nanoparticles in the cellular environment, indicating their excellent biostability. Moreover, even after laser application, none of the nanoparticles degraded but instead underwent reshaping into a more crystalline structure.

[1] Université de Technologie de Compiègne, ESCOM, TIMR (Integrated Transformations of Renewable Matter), Centre de Recherche Royallieu, CS 60 319-60 203, Compiègne, Cedex, France. [2] Laboratoire Physico Chimie Curie, CNRS UMR168, Institut Curie, Sorbonne Université, PSL University, 75005 Paris, France. [3] Departamento de Electrocerámica, Instituto de Cerámica y Vidrio, ICV-CSIC, C/ Kelsen 5, 28049 Madrid, Spain. [4] Université Sorbonne Paris Nord, Université Paris Cité, Laboratory for Vascular Translational Science, LVTS, INSERM, UMR 1148, F—93017 Bobigny, France. [5] Département de Biophysique et de Médecine Nucléaire, Assistance Publique-Hôpitaux de Paris, Hôpital Avicenne, F 93009 Bobigny, France. [6] Instituto de Ciencia de Materiales de Madrid, Consejo Superior de Investigaciones Científicas, c/ Sor Juana Inés de la Cruz, 3, 28049 Madrid, Spain. [7] IMDEA Nanociencia, c/ Faraday 9, 28049 Madrid, Spain. [8] These authors contributed equally: Erwann Guénin, Alexandre Fromain. ✉email: claire.wilhelm@cnrs.fr

The use of photo-responsive nanoparticles for photothermal therapy (PTT) is becoming increasingly popular in cancer treatment, as it combines effectiveness, on-demand action, and remote stimulation. Among the various nano-heaters reported, Au-based nanoparticles are considered the gold standard due to their excellent stability and intense plasmonic resonance, which can be tuned to the near-infrared (NIR) biological window by adjusting the shape of the nanoparticles, such as nanorods[1] or nanostars[2]. Other nanomaterials, such as iron oxides, have emerged as robust alternatives for inducing an anticancer photothermal effect[3–6]. Additionally, the field of nanomedicine is constantly incorporating other nanoparticle compositions[7], including platinum (Pt), which offer a range of applications in imaging[8–10], detection[11,12], or therapy[13–15]. Pt nanoparticles are particularly attractive candidates for therapeutic action because of their high atomic number (78), which allows them to act as radiosensitizers and enhance the effectiveness of radiotherapy by improving the absorption of ionic radiation energies[16–18].

It is worth noting that the cis-platinum complex [Pt(NH$_3$)$_2$Cl$_2$], which is commonly used as chemotherapy for the treatment of various cancers (including lung, ovarian, testicular, and lymphoma), is based on Pt (II). However, the mechanism of action is linked to the complex, which acts by alkylation of DNA and transcription inhibition, rather than the metallic Pt itself. Nevertheless, Pt nanoparticles have been considered as potential initiators for a chemo-therapeutic effect[19–25]. The hypothesis of using Pt nanoparticles as initiators for a chemo-therapeutic action is double-edged, as it suggests an inherent cytotoxicity of Pt nanoparticles, which could be mediated by the release of reactive Pt-based species. However, recent studies have reported that Pt nanoparticles offer good cytocompatibility and in vivo tolerance, without causing any significant toxicity[26–30].

It is also noteworthy to mention that emerging strategies in the field of nanomedicine are currently focused on intracellular nano-degradation of nanoparticles (for instance Fe-based[31–35], but also FePt[36–39]) to elicit therapeutic action via the release of cytotoxic reactive species. Certain works are even considering the triggering or acceleration of nanoparticle degradation through external stimuli such as laser irradiation[40–43]. In light of these developments, Pt nanoparticles appear to be a potential candidate for merging PTT and chemotherapy, due to their potential for releasing reactive Pt-based species upon intracellular degradation, which could enhance the therapeutic effect.

However, the plasmonic resonance of Pt is primarily in the ultraviolet region[44,45], which implies that Pt nanoparticles may not be the preferred choice for photothermal applications in the NIR window of nanomedicine. Despite this, a few studies have reported successful PTT applications of Pt nanoparticles under NIR irradiation[26,46].

This study aims to integrate the recent field of Pt nanoparticles for nanomedicine, with a particular emphasis on designing nanoparticles for optimized photothermal conversion and evaluating their intracellular stability both with and without laser irradiation. The proposed Pt-based nanomaterials have a raspberry-like multi-core structure and are produced using a one-pot methodology that involves coating and assembling with alendronate. The significance of a multi-core structure has been previously demonstrated with Au-based NanoRaspberries[47], which can shift their absorbance towards the NIR. Therefore, dendritic-shaped nanoparticles are considered to have promising characteristics for biomedical applications due to their distinct physicochemical, optical, and electronic properties[48–50].

In this study, we put forward and demonstrate the hypothesis that confining a large number of Pt cores can also have a beneficial effect on PTT. We also systematically compare the effects of Pt multi-core NanoRaspberries (NR) and single-core ultrasmall Pt NanoSeeds (NS), on PTT for glioblastoma cancer spheroids. Additionally, we used X-ray absorption spectroscopy (XAS) at the Pt L$_3$-edge (11,564 eV) to analyze the atomic and electronic structure of both nanoparticles, their behavior after being internalized in the cellular environment, as well as their stability after laser exposure. This assessment of nanomaterial stability is a crucial factor to consider for their potential therapeutic use.

Results and discussion

Synthesis and characterization of Pt nanoparticles. The synthesis of Pt nanoparticles involves the combination of an aqueous Pt(II) solution with sodium ascorbate, which acts as a reducing agent, along with a stabilizing solution of biphosphonate (alendronate) in either acidic (pH 3) or basic (pH 10) conditions. The formation of nanoparticles is facilitated by microwave treatment at 100 °C for 30 min. Under alkaline conditions, alendronate acts as a coating agent, resulting in the formation of ultra-small nanoparticles (referred to as NanoSeeds or NS) as shown in Fig. 1A. On the other hand, acidic pH causes alendronate to assemble the NanoSeeds together, leading to the formation of multi-core structures (referred to as NanoRaspberries or NR) as illustrated in Fig. 1B. NS have a mean diameter of 1.8 ± 0.3 nm, as determined from size measurements on transmission electron microscopy (TEM) images (Fig. 1C). In contrast, assembled NR have an average size of 69 ± 10 nm (Fig. 1D). Absorbance spectra of both types of nanoparticles show a decreasing trend from 300 to 800 nm (Fig. 1E). Notably, the absorbance of NR is higher than that of NS, with a 1.5-fold increase at 300 nm and a 3-fold increase in the NIR region at 800 nm. The structure of the nanoparticles was further analyzed using X-ray absorption spectroscopy (XAS), specifically focusing on the Pt L$_3$-edge. The X-ray absorption near-edge structure (XANES) spectra of NS and NR at the Pt L$_3$-edge (Fig. 1F, G) reveal that NS are partially oxidized compared to the Pt foil, while NR are more oxidized than NS. This is evident from the whiteline intensity and whiteline width in the normalized XANES spectra[51] (Fig. 1F) as well as the shift of the first derivative maximum around 11568.5 eV in Fig. 1G, indicating that NR have the highest level of oxidation. This could be attributed to the synthesis of NR in an acidic environment. Moreover, a flattened post-edge resonance after the whiteline is observed for NS, and it is most prominent for NR, which suggests local disordering due to Pt oxidation[52]. Changes in the valence of the absorbing atom, as indicated by whiteline variations, are often accompanied by changes in structure, coordination, bond length, and disorder, as well as variations in particle size or induced strain[53]. These transformations are further investigated using extended X-ray absorption fine structure (EXAFS) analysis, as shown in Fig. 1H and Table 1. For NS, in addition to the Pt-Pt shell at a similar position as the Pt foil (around 2.7 Å), a new shell corresponding to Pt-O bonds at 1.9 Å, indicative of Pt oxide character, is observed. This Pt oxide character becomes more pronounced in NR. Furthermore, an increase in the Debye-Waller factor (related to local structural disorder) with the oxide fraction is observed, confirming the results obtained from XANES analysis. Figure 1I illustrates the heating cycles of both nanoparticles dispersed in water at a concentration of [Pt] = 6.7 mM when subjected to an 808 laser with an output power 1.65 W. This power corresponds to an average power density of 1 W cm^{-2} at a distance of 4 cm from the laser fiber. The light-to-heat conversion efficiency was determined using the methodology described in the Methods section. The calculated values for the photothermal conversion efficiency were found to be η = (16 ± 3) % for NS and η = (25 ± 4) % for NR. Pt-based nanoparticles certainly do not perform better than gold-based ones, such as gold nanorods, that have already undergone extensive validation for
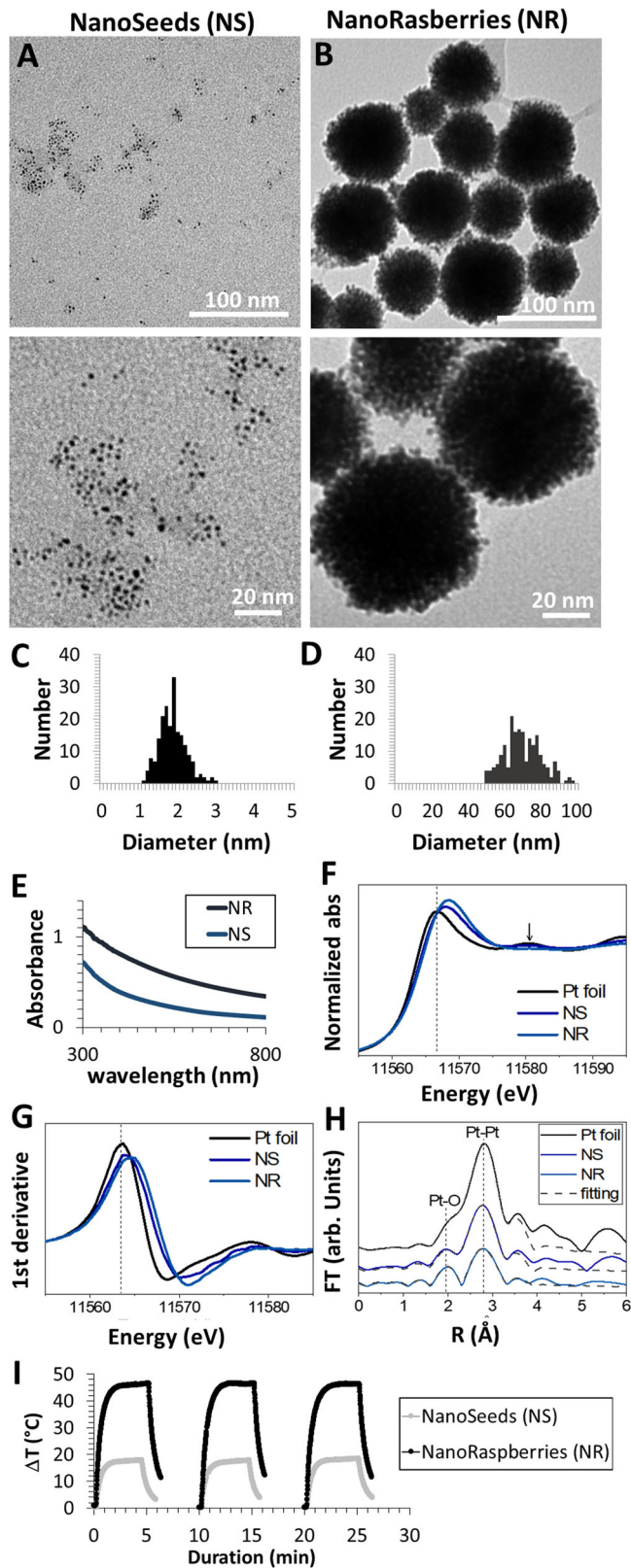
NanoSeeds (NS)   NanoRasberries (NR)

Fig. 1 Analysis of Pt-base nanoparticles. A Transmission electron microscopy images of NS, with larger view at the bottom; **B** Transmission electron microscopy images of NR, with larger view at the bottom; **C** NS size distribution analyzed on 200 independent nanoparticles on TEM images; **D** NR size distribution analyzed on 200 independent nanoparticles on TEM images; **E** Absorbance of NS and NR at the same Pt concentration; **F** XANES spectra at the Pt L$_3$-edge for Pt NS and Pt NR compared with Pt foil. **G** First derivative of the XANES spectra to corroborate the changes in oxidation state. **H** Fourier transform (FT) of EXAFS signal for Pt foil, Pt NS and Pt NR. **I** Heating curves of NS and NR dispersed in water at [Pt] = 6.7 mM and irradiated with an 808 nm laser beam at an output power of 1.65 W (average power density of 1 W cm^{-2}). Three 10 min laser on/off cycles are provided that prove the stability of the nanoparticles upon heating.

Table 1 Results of the EXAFS fittings of Pt foil together with NS and NF samples at Pt-L$_3$ absorption edge.

Sample	Shell	N	R (Å)	DW (Å^2)
Pt foil	Pt-Pt	12	2.761(2)	0.003(1)
NS	Pt-O	1.1(1)	1.97(3)	0.031(8)
	Pt-Pt	9.6(1)	2.752(2)	0.007(1)
NR	Pt-O	2.1(1)	1.93(3)	0.012(3)
	Pt-Pt	8.3(2)	2.774(8)	0.003(1)
Cells-NS-D1	Pt-X	–	2.40(3)	0.008(2)
Cells-NS-D1-LASER	Pt-X	–	2.42(5)	0.005(2)
Cells-NS-D12	Pt-X	–	2.39(3)	0.008(3)
Cells-NS-D12-LASER	Pt-X	–	2.36(4)	0.006(3)
Cells-NR-D1	Pt-Pt	5.3(3)	2.749(4)	0.005(1)
Cells-NR-D1-LASER	Pt-Pt	8.9(2)	2.756(6)	0.008(2)
Cells-NR-D12	Pt-Pt	5.0(2)	2.750(3)	0.006(1)
Cells-NR-D12-LASER	Pt-Pt	9.6(3)	2.750(2)	0.007(1)

X = P, S.
N coordination number, R interatomic distance, DW Debye-Waller factor.

Cell internalization of Pt NS and Pt NR and photothermal heating effect.

Glioblastoma cancer cells (U87) were then exposed to the Pt nanoparticles at varying concentrations ranging from [Pt] = 0.2 mM to 1.25 mM for 24 h. Afterward, the cells were fixed, processed for TEM, and imaged for different incubation conditions. For both nanoparticles NS and NR, images were taken for incubation conditions of [Pt] = 0.2 mM (Fig. 2A for NS, Fig. 2C for NR) and [Pt] = 0.5 mM (Fig. 2B for NS, Fig. 2D for NR). The images reveal that both types of Pt nanoparticles are internalized by the cells through endocytosis and consistently localize within endosomes. The number of endosomes filled with nanoparticles per cell increases with the administered dose. In the case of NR, several nanoparticles can be found within the same endosome, ranging from 1 to 5 nanoparticles. On the other hand, for NS, the nanoparticles appear to be highly aggregated within each endosome.

The amount of Pt internalized by the cells was quantified using atomic emission spectroscopy (ICP-AES) on cell lysates. The results showed that it ranged from 0.1 to 1 pg of Pt per cell, and was similar for both Pt NS (Fig. 3A) and Pt NR (Fig. 3B).

To evaluate the photothermal heating effect of Pt-loaded cells, the cells were arranged in a 3D tumoroid-like configuration, which is closer to the solid tumors in vivo compared to 2D monolayers. To form the spheroids, 200,000 cells loaded with different doses of Pt NS and Pt NR were aggregated by centrifugation and allowed to mature in a 0.5 mL tube in complete medium for 2 days, forming compact spheroids resembling tumoroids (Fig. 3C, D). Photothermal measurements

photothermal therapy. Yet, while gold nanorods production[54] generally involves a multistep protocol with the use of hexadecyltrimethylammonium bromide (CTAB) and AgNO$_3$ that could pose biocompatibility issues, the Pt-based nanoparticles investigated here are synthesized in 30 min in water using alendronate only, a molecule already FDA approved for osteoporosis on g daily basis.
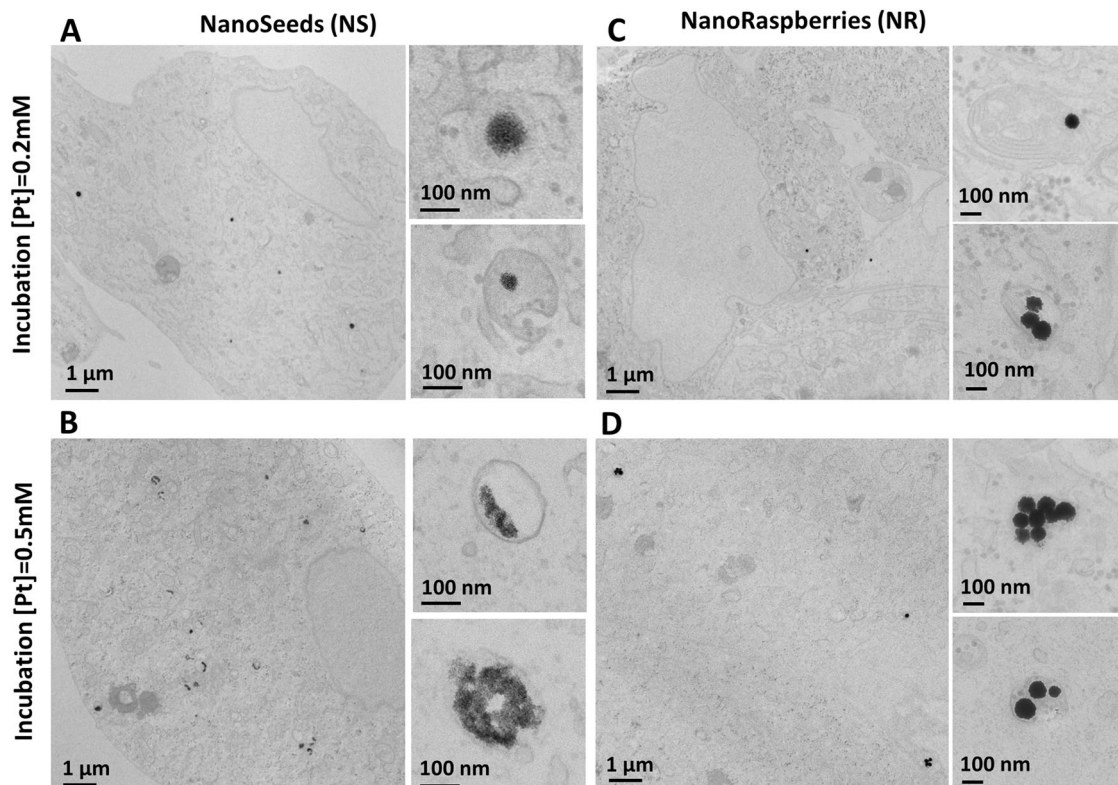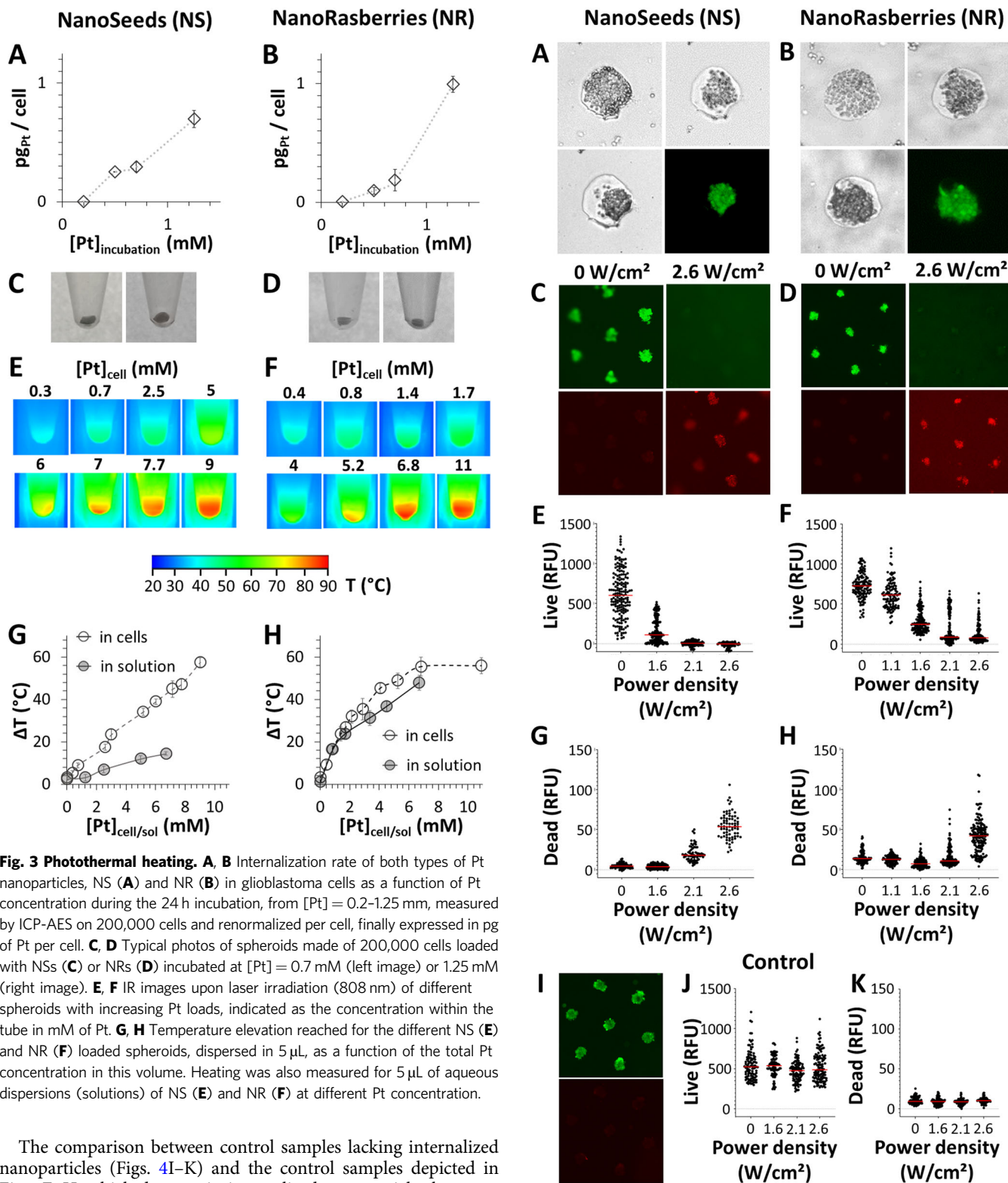
Fig. 2 Intracellular localization of the nanoparticles. Transmission electron microscopy images of cells having internalized Pt NS at [Pt] = 0.2 mM (**A**) or [Pt] = 0.5 mM (**B**) and Pt NR at [Pt] = 0.2 mM (**C**) and [Pt] = 0.5 mM (**D**).

were then performed using an 808 nm laser at the single spheroid level, in the tube, with a total volume of 5 μL, which was sufficient to cover the spheroid. The Pt concentration in the samples was calculated by dividing the quantity of Pt in the spheroids (as measured by ICP) by the volume of 5 μL. Aqueous dispersions of nanoparticles were also prepared in the same 5 μL volumes at different concentrations to compare heating in cells and in water. The samples were irradiated with an 808 nm laser beam with an output power of 1.65 W, which corresponds to an average power density of 1 W cm^{-2}, but increases to 2.6 W cm^{-2} at the center of the tube due to the Gaussian distribution of the beam. Infra-red camera was used for temperature mapping (Fig. 3E, F). Temperature elevations were averaged in Fig. 3G (NS) and 3H (NR) for the different concentrations tested. The results showed that NS are not efficient for photothermal heating in solution, but they start heating efficiently when confined in cells. In contrast, NR exhibit the same high photothermal conversion both in cells and in water. These measurements clearly demonstrate that NR are efficient photothermal agents due to their multi-core structure mediated by alendronate aggregation, and their heating capabilities remain unchanged in the intracellular environment, making them suitable for heating both the cancer cell environment (extracellular heating) and the cells themselves (intracellular heating). However, the situation is different for NS, which exhibit low heating in solution (and thus in the extracellular environment), but become almost as efficient as NR when located inside the cells due to massive aggregation within the endosomes. Of course, for this aggregation effect to yield beneficial results in vivo, a substantial quantity of nanoparticles must successfully penetrate the cancer cells, uneasily attainable after intravenous injection. However, this is precisely where NR exhibit their distinctive advantage. By controlling the aggregation process prior to in vivo administration, they enable optimization of photothermal conversion efficiency upstream, independent of

achieving a specific dosage within the target cancer cells. This pre-administration control over aggregation thus holds potential for enhancing the effectiveness of the Pt-based nanoparticles in vivo.

High-throughput photothermal treatment on spheroids in microwells. Next step was to evaluate the photothermal therapy of glioblastoma cells with the two types of nanoparticles. To do so, the live/dead assay was used to quantify both the viability and the death of spheroids after laser treatment. In order to have a significant number of spheroids, and the possibility for fluorescence imaging (live cells in green/dead cells in red) at spheroid level, spheroids were grown in 200 μm diameter microwells fabricated in agarose inside each well of a 96-well plate. 500 cells loaded with the nanoparticles were deposited in each microwell by centrifugation. After two days of maturation, all microwells were containing 100 μm diameter live spheroids (Fig. 4A for NS-loaded cells and Fig. 4B for NR-loaded cells). The entire wells of the plate could then be irradiated sequentially with the laser, for 5 min. To do so, the laser beam was adjusted the well diameter. Figure 4C, D show typical fluorescence imaging of the spheroids in microwells for NS-loaded cells (Fig. 4C) and NR-loaded cells (Fig. 4D), without laser treatment (0 W cm^{-2}) and for the maximal laser power density (2.6 W cm^{-2}) showing the two extreme cases of live only spheroids or dead only ones. Figure 4E–H finally present the live and dead fluorescence measured for all spheroids ($n > 100$) irradiated with different laser power density. It shows similar efficiency in terms of cell death induction for both NS and NR, in line with their similar heating once in the cells. For both, cell death is almost total for laser power density of 2.1 and 2.6 W cm^{-2}. Importantly, for spheroids made of unlabeled (control) cells, no increase of cell death is detected, whatever the laser power density (Fig. 4I–K).

Fig. 3 Photothermal heating. A, **B** Internalization rate of both types of Pt nanoparticles, NS (**A**) and NR (**B**) in glioblastoma cells as a function of Pt concentration during the 24 h incubation, from [Pt] = 0.2–1.25 mm, measured by ICP-AES on 200,000 cells and renormalized per cell, finally expressed in pg of Pt per cell. **C**, **D** Typical photos of spheroids made of 200,000 cells loaded with NSs (**C**) or NRs (**D**) incubated at [Pt] = 0.7 mM (left image) or 1.25 mM (right image). **E**, **F** IR images upon laser irradiation (808 nm) of different spheroids with increasing Pt loads, indicated as the concentration within the tube in mM of Pt. **G**, **H** Temperature elevation reached for the different NS (**E**) and NR (**F**) loaded spheroids, dispersed in 5 µL, as a function of the total Pt concentration in this volume. Heating was also measured for 5 µL of aqueous dispersions (solutions) of NS (**E**) and NR (**F**) at different Pt concentration.

The comparison between control samples lacking internalized nanoparticles (Figs. 4I–K) and the control samples depicted in Fig. 5E–H, which do contain internalized nanoparticles but were not subjected to laser application (0 W cm^{-2}), also serves as evidence that the Pt-based nanoparticles by themselves do not induce any cell death. Indeed, the occurrence of cell death could have been expected due to the enzymatic catalytic activity of Pt that could have catalyzed toxic superoxide radicals from hydrogen peroxide present in tumor cells.

Biostability evaluation. The final step was to determine the biostability of the Pt nanostructures once in the intracellular

environment. XAS at the XANES and EXAFS regimes can provide unique in situ description of the local electronic and atomic structure of nanomaterials in their environment, possibly biological. XAS measurements were thus performed on spheroids either at day 1 after their formation, or 12 days later (day 12), and compared with the spectra in aqueous dispersion. Besides, other spheroids that had been laser irradiated were also measured, at both day 1 and day 12 to assess the effect of laser irradiation at structural level.

Fig. 4 High-throughput evaluation of cell death at spheroid level after photothermal treatment. A, **B** Growth of spheroids in microwells starting from 250 cells loaded with Pt NS (**A**) or Pt NR (**B**). Images are shown at day 0 (seeding), and day 1 and day 2 of maturation. At day 2, live staining (green) is included. **C**, **D** Live (green) and dead (red) images at day 2 of the microwell array containing the NS (**C**) and NR (**D**) loaded spheroids, without (0 W cm⁻²) and with (2.6 W cm⁻²) laser exposure.
E–**H** Quantification on single spheroids of the live and dead signal as a function of the laser power density: (**E**) and (**F**) correspond to the live fluorescent signal of NS and NR loaded spheroids, respectively; (**G**) and (**H**) correspond to the dead fluorescent signal of NS and NR loaded spheroids, respectively. **I**–**K** Quantification of the live and dead signal of spheroids formed of unlabeled (control) cells; (**I**) live (green) and dead (red) staining for spheroids exposed to the highest laser power density of 2.6 W cm⁻². **J**, **K** correspond to respectively the live and dead fluorescent signal for all measured spheroids, as a function of the laser power density.

XANES spectra for all conditions are shown for NS and NR in Fig. 5A, B, respectively. NS in the intracellular environment after day 1 shows a change in the XANES response with respect to the solution, both in the position of the whiteline towards that of the Pt foil and in the resonances that follow, indicating a change in the environment of the Pt absorbing atoms. After day 12 no XANES variations are identified compared with day 1 while a whiteline decrease is identified for the irradiated nanostructures. For the NR system, XANES results show a reduction of the Pt atoms as NR are internalized after day 1 and day 12 (similar absorption signal), with the whiteline at positions of the Pt foil but a lower intensity and a similar XANES spectra. After laser irradiation, an intensity increase of whiteline is obtained for both cases with a higher intensity after day 12. In any situation, the whiteline intensity are lower than that of the Pt foil. Those modifications of whiteline intensity could be attributed to some electron transfer or/and coordination modifications[55]. The Fourier transform (FT) of the EXAFS signal are then shown in Fig. 5C, D, to investigate the distributions of atoms within the nanoparticles, without and with laser irradiation and compared with the aqueous dispersion, at day 1 and day 12 for NS (Fig. 5C) and NR (Fig. 5D), respectively). For NS system for all conditions, a shift of the first shell at lower position with respect to the solution is obtained falling around 2.4 Å, confirming the change in the environment around the Pt atoms after the internalizations into cells. Different scenarios are considered and the EXAFS signal is fitted considering the Pt atoms coordinated with P and/or S atoms. This structural variation could be related with the heating efficacy of nanostructures in the cell environment and not in aqueous dispersion. For NR into the cell for all conditions, just one shell is obtained at positions close to that of the Pt shell around 2.8 Å with lowest intensity related to the coordination. After the laser irradiation, an increase of coordination is obtained for both day 1 and day 12, being higher for the latter. Remarkably, not only these measures evidence no degradation of the nanoparticles, but it shows on the contrary a biotransformation towards metallic Pt for NR and some compound with Pt-S/P coordination at short order for NS inside the cells. And last but not least, no significant structural change is identified. Just a change in the coordination number increasing it is detected, which could be related to a marked increase of the crystallinity.

At this stage, we cannot definitively determine the long-term in vivo stability. However, we have observed that there is no degradation at the spheroid-tissue level over a period of approximately two weeks. In contrast, significant degradation was observed when using a similar spheroid model with nanoparticles made of iron oxide[56], silver[57], or copper sulfide[58]. Interestingly, gold nanoparticles also did not degrade at all[57,59],
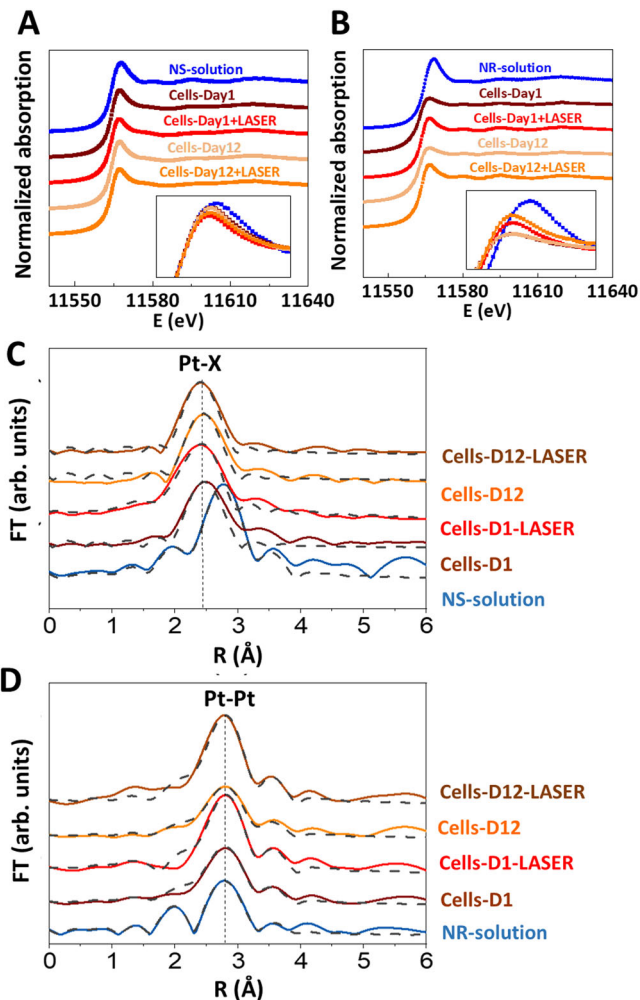

Fig. 5 Intracellular stability of the local electronic and atomic structure investigated with XANES and EXAFS. Normalized XANES spectra of solution and cells without and with laser application, at day 1 or day 12 of spheroids maturation, are shown for NS (**A**) and NR (**B**). Insets show a detailed view of whiteline changes. FTs of the EXAFS signals are shown for spheroids at day 1 and day 12 without or after laser exposure, for NS (**C**) and NR (**D**).

suggesting that Pt behaves similarly to Au based on these initial in vitro observations. However, it will be essential in the future to investigate this similarity in terms of both long-term in vivo stability and efficiency. Additionally, it is yet to be explored whether it would be advantageous to utilize nanomaterials that can degrade over time and be cleared out after accomplishing their therapeutic mission, despite the risk of triggering a biological response through the release of ionic species. Alternatively, nanoparticles that remain intact inside the cells for an extended period of time may also be considered.

Conclusion

The new class of Pt multi-core raspberries-like nanoparticles alendronate-assembled were efficiently internalized in cancer cells and provided sufficient heating to kill cancer spheroids upon laser exposure. These Pt NanoRasbperries (NR) were compared to ultrasmall Pt nanoparticles, NanoSeeds (NS), similar to the cores composing the Pt NR. While NR photothermal conversion was much higher that NS one for nanoparticles in aqueous dispersion, once confined within the endosomes of the cancer cells, NS were almost as efficient nano-heaters than NR, confirming the

importance of aggregation in photothermal conversion. The Pt biostability of both nanoparticles was excellent, as revealed by XAS, after 1 day or 12 days of cellular processing. Remarkably, even after laser application, none were degrading, but conversely, were reshaped into more crystalline structure. To conclude, Pt nanoparticles with multi-core design appear as promising photothermal therapeutic agents both in the extracellular and intracellular environments, without triggering any degradation, even by laser irradiation.

Materials and methods

Synthesis of Pt nanoparticles. The multi-core synthesis is similar to previously reported ones based on Au[47] or Pd[60]. 80 μL of 20 mM potassium tetrachloroplatinate at 20 mM and 180 μL of alendronate at 40 mM were mixed in 2 mL ultrapure water, at pH 3 or pH 10. 40 μL of a sodium ascorbate (17.6 mg/mL) were then added and the mix was microwave-heated (Monowave 300, Anton Paar GmbH) for 30 min at 80 °C. The solutions containing the nanoparticles were finally dialyzed (Spectra.Por Float-A-Lyzer G2) and were ready for use.

Cell culture and nanoparticles incubation. U-87 MG human glioblastoma cells (ATCC) were grown in Dulbecco's Modified Eagle Medium (DMEM) supplemented with 10% fetal bovine serum and 1% penicillin-streptomycin in a humidified incubator with 5% CO_2 at 37 °C. After reaching 80% confluence, the cell culture medium was replaced by a solution of nanoparticles dispersed in complete culture medium at concentrations [Pt] = 0.2, 0.5, 0.7, and to 1.25 mM. Cells were left to incubate for 24 h. They were then rinsed twice with complete medium and detached using 0.05% trypsin-EDTA solution. After cell counting, 200,000 cells were centrifuged at 1100 rpm for 5 min in 1 mL of culture medium in a 15 mL Falcon tube. The pellet is left in the incubator in tubes with partially open cap to mature for one or two days and consistently formed a cohesive spheroid in 1 day.

Transmission electron microscopy. For nanoparticles imaging, 10 μl of diluted nanoparticles suspension were seeded on 200 mesh copper, left for 1 min, and then dried with absorbing paper. For imaging inside the spheroids, they were processed as follows. Spheroids were washed with cacodylate buffer (0.2 M), then fixed with 5% glutaraldehyde in 0.1 M cacodylate buffer for 1 h min at room temperature and rinsed again in the same cacodylate buffer (0.2 M). The samples were then contrasted with Oolong Tea Extract (OTE) diluted to 0.5% in cacodylate buffer, and post-fixed in 1% osmium tetroxide containing 1.5% potassium cyanoferrate and dehydrated in increasing ethanol baths. Samples were then embedded in Epon epoxy resin, sectioned (70 nm) and placed on a copper grid for observation. All nanoparticles and cell samples were observed with a HITACHI HT 7700 electron microscope operating at 120 kV (INRA, France).

Pt quantification by ICP-AES. The total amount of platinum in the cell samples was determined by ICP-AES (inductively coupled plasma atomic emission spectroscopy - Spectrogreen, SPECTRO). For each measurement, the number of cells was counted using a Malassez chamber, and the samples were digested with aqua regia consisting of a mixture of hydrochloric acid (2/3) and nitric acid (1/3). The mixture was then placed on a hot plate for evaporation, then re-suspended in 200 μL of hydrochloric acid and left at room temperature for two days. This final solution was then diluted with ultra-pure filtered water to reach 2% HCl solution, before measuring the total amount of Pt by ICP-AES.

Photothermal heating by 808 nm laser application. The heating profile was systematically acquired in 5 μL volume at the bottom of 0.5 mL Eppendorf tubes.

For aqueous dispersions, the solutions were diluted at different concentrations ranging from [Pt] = 0.125 to 6.7 mM. For spheroids, they were placed in tubes, and total volume was adjusted to 5 μL. A 808 nm laser was used (Laser Components). The laser beam was positioned at a distance of 4 cm from the liquid surface, and the output laser was set at 1.65 W. This corresponded to a mean power density of $1\,W\,cm^{-2}$ in the sample plane. However, the laser beam has a gaussian profile and at the center of it, where the sample is located, the power density is higher, measured with mask and powermeter at $2.6\,W\,cm^{-2}$. The temperature elevation was measured in real time using an infrared thermal camera (FLIR A615) and data were processed with the FLIR ResearchIR software. The light-to-heat conversion coefficient is calculated from heating curves[61], as $\eta = B.\Delta T.\frac{m_{sample}C_w}{P_0(1-10^{-A})}$ with the sample mass m_{sample} approximated to the mass of water, C_w the specific heat capacity ($4.18\,J\,g^{-1}\,K^{-1}$), P_0 the incident laser power and A the absorbance of the sample. B, the rate of heat dissipation, is calculated from the decreasing temperature curves when the laser is turned off, $B = \frac{-1}{t}.\ln\left(\frac{T(t)-T_0}{T_m-T_0}\right) = 0.025 s^{-1}$.

Photothermal therapy on spheroids in microwells. U87 cells incubated with [Pt] = 0.7 mM of NS and NR for 24 h in complete DMEM medium were detached and deposited in wells of 96-well plate (20,000 cells per well) containing agarose molded microwells. Those microwells were microfabricated thanks to 3D printed stamps containing a network of micro-pillars (37) of 200 μm diameter and 200 μm height. In all, 50 μL of liquid 2% agarose in PBS was poured in each well, the stamps were placed, and the agarose was left to solidify (15 min) before removing the stamps. Cells deposited in well were centrifuged (1200 rpm, 3 min) to fall within the microwells (500 cells per microwell). They were left to mature into cohesive spheroids for 2 days before laser application, performed in situ of the 96-well plate containing the microwells. The laser was adjusted at 3 cm above the plate surface with a laser holder centered on top of each well. Laser power density as calibrated with a mask of the well surface, positioned at 3 cm. 4 power densities of 1.1, 1.6, 2.1, and $2.6\,W\,cm^{-2}$ were selected, and applied well per well, for 5 min in a 37 °C - 5% $C0_2$ environment. Live/Dead staining was performed after laser irradiation according to supplier instructions (LIVE/DEAD™ Cell Imaging Kit R37601, Invitrogen™). Multi-well images were acquired in fluorescence mode with EnSight Microplate Reader (Perkin Elmer). Images were processed with ImageJ.

X-ray absorption spectroscopy. Both the X-ray absorption near-edge structure (XANES) and X-ray absorption fine structure (EXAFS) experiments were performed on samples at the BL22 CLÆSS beamline of the ALBA synchrotron facility in Cerdanyola del Vallès (Spain)[62]. Measurements were achieved at room temperature in fluorescence mode at the Pt L_3-edge (11564 eV). The monochromator used in the experiments was a double Si crystal oriented in the (311) direction. Pt metal foil was measured and used to calibrate the energy. Solutions and cells were measured in transmission or fluorescence configuration, according to convenience, in order to have an absorption jump of 1. The XAS analysis was performed using the Athena and Artemis softwares[63].

The modulus of the Fourier transform (FT) of the EXAFS signal at the Pt L_3-edge is performed in the $k^2\chi(k)$ weighted EXAFS signal between 2.4 and 9.0 Å^{-1}. Experimental EXAFS results are fitted in R-space in the range 1.4–3.5 Å using the

FEFFIT code[64]. The fitting was performed by fixing the shift at the edge energy E_0 and using the number coordination N, the interatomic distance R and the Debye-Waller (DW) factors as free parameters.

Data availability

References

1. Huang, X., El-Sayed, I. H., Qian, W. & El-Sayed, M. A. Cancer cell imaging and photothermal therapy in the near-infrared region by using gold nanorods. *J. Am. Chem. Soc.* **128**, 2115–2120 (2006).
2. Arami, H. et al. Remotely controlled near-infrared-triggered photothermal treatment of brain tumours in freely behaving mice using gold nanostar s. *Nat. Nanotechnol.* **17**, 1015–1022 (2022).
3. Estrader, M., Soulantica, K. & Chaudret, B. Organometallic synthesis of magnetic metal nanoparticles. *Angew. Chem. Int. Ed.* **61**, e202207301 (2022).
4. Sharma, S., Shrivastava, N., Rossi, F. & Thanh, N. T. K. Nanoparticles-based magnetic and photo induced hyperthermia for cancer treatment. *Nano Today* **29**, 100795 (2019).
5. Kasparis, G. et al. Zn doped iron oxide nanoparticles with high magnetization and photothermal efficiency for cancer treatment. *J. Mater. Chem. B* **11**, 787–801 (2023).
6. Bertuit, E. et al. Structure–property–function relationships of iron oxide multicore nanoflowers in magnetic hyperthermia and photothermia. *ACS Nano* **16**, 271–284 (2021).
7. Zhang, W., Bojdys, M. & Pinna, N. A universal synthesis strategy for tuneable metal-organic framework nanohybrid. *Angew. Chem. Int. Ed.* **62**, e202301021 (2023).
8. Chen, D. et al. One-step rapid synthesis of fluorescent platinum nanoclusters for cellular imaging and photothermal treatment. *RSC Adv.* **4**, 40141–40145 (2014).
9. Chen, D. et al. In situ biosynthesis of fluorescent platinum nanoclusters: toward self-bioimaging-guided cancer theranostics. *ACS Appl. Mater. Interfaces* **7**, 18163–18169 (2015).
10. Zheng, X., Chen, W., Cui, P., Wang, Z. & Zhang, W. Design of multifunctional FePt/GO nanocomposites for targeting, dual-modal imaging diagnostic and in situ therapeutic potential theranostic platform. *RSC Adv.* **4**, 58489–58494 (2014).
11. Higuchi, A. et al. Preparation of a DNA Aptamer− Pt complex and its use in the colorimetric sensing of thrombin and anti-thrombin antibodies. *Anal. Chem.* **80**, 6580–6586 (2008).
12. Taurino, I. et al. Fast synthesis of platinum nanopetals and nanospheres for highly-sensitive non-enzymatic detection of glucose and selective sensing of ions. *Scientific Rep.* **5**, 15277 (2015).
13. Moglianetti, M. et al. Platinum nanozymes recover cellular ROS homeostasis in an oxidative stress-mediated disease model. *Nanoscale* **8**, 3739–3752 (2016).
14. Hosaka, H., Haruki, R., Yamada, K., Böttcher, C. & Komatsu, T. Hemoglobin–albumin cluster incorporating a Pt nanoparticle: artificial O2 carrier with antioxidant activities. *PLoS ONE* **9**, e110541 (2014).
15. Shibuya, S. et al. Palladium and platinum nanoparticles attenuate aging-like skin atrophy via antioxidant activity in mice. *PLoS ONE* **9**, e109288 (2014).
16. Bergs, J. W. et al. The role of recent nanotechnology in enhancing the efficacy of radiation therapy. *Biochim. Biophys. Acta (BBA)-Rev. Cancer* **1856**, 130–143 (2015).
17. Bao, Z. et al. FePt nanoparticles: a novel nanoprobe for enhanced HeLa cells sensitivity to chemoradiotherapy. *RSC Adv.* **6**, 35124–35134 (2016).
18. Li, Q., Tanaka, Y., Saitoh, Y., Tanaka, H. & Miwa, N. Carcinostatic effects of platinum nanocolloid combined with gamma irradiation on human esophageal squamous cell carcinoma. *Life Sci.* **127**, 106–114 (2015).
19. Kutwin, M. et al. Investigation of platinum nanoparticle properties against U87 glioblastoma multiforme. *Arch. Med. Sci.* **13**, 1322–1334 (2017).
20. Gao, J. et al. FePt@ CoS2 yolk− shell nanocrystals as a potent agent to kill HeLa cells. *J. Am. Chem. Soc.* **129**, 1428–1433 (2007).
21. Asharani, P., Xinyi, N., Hande, M. P. & Valiyaveettil, S. DNA damage and p53-mediated growth arrest in human cells treated with platinum nanoparticles. *Nanomedicine* **5**, 51–64 (2010).
22. Chien, C. T. et al. Caged Pt nanoclusters exhibiting corrodibility to exert tumor-inside activation for anticancer chemotherapeutics. *Adv. Mater.* **25**, 5067–5073 (2013).
23. Buchtelova, H. et al. Size-related cytotoxicological aspects of polyvinylpyrrolidone-capped platinum nanoparticles. *Food Chem. Toxicol.* **105**, 337–346 (2017).
24. Alshatwi, A. A., Athinarayanan, J. & Vaiyapuri Subbarayan, P. Green synthesis of platinum nanoparticles that induce cell death and G2/M-phase cell cycle arrest in human cervical cancer cells. *J. Mater. Sci.: Mater. Med.* **26**, 1–9 (2015).
25. Shiny, P., Mukherjee, A. & Chandrasekaran, N. DNA damage and mitochondria-mediated apoptosis of A549 lung carcinoma cells induced by biosynthesised silver and platinum nanoparticles. *RSC Adv.* **6**, 27775–27787 (2016).
26. Samadi, A. et al. Platinum nanoparticles: a non-toxic, effective and thermally stable alternative plasmonic material for cancer therapy and bioengineering. *Nanoscale* **10**, 9097–9107 (2018).
27. Gatto, F., Moglianetti, M., Pompa, P. P. & Bardi, G. Platinum nanoparticles decrease reactive oxygen species and modulate gene expression without alteration of immune responses in THP-1 monocytes. *Nanomaterials* **8**, 392 (2018).
28. Shoshan, M. S., Vonderach, T., Hattendorf, B. & Wennemers, H. Peptide-coated platinum nanoparticles with selective toxicity against liver cancer cells. *Angew. Chem. Int. Ed.* **58**, 4901–4905 (2019).
29. Gulino, M., Santos, S. D. & Pêgo, A. P. Biocompatibility of platinum nanoparticles in brain ex vivo models in physiological and pathological conditions. *Front. Neurosci.* **15**, 787518 (2021).
30. Sancho-Albero, M. et al. Exosomes loaded with ultrasmall Pt nanoparticles: a novel low-toxicity alternative to cisplatin. *J. Nanobiotechnol.* **20**, 1–14 (2022).
31. Bao, W. et al. Nanolongan with multiple on-demand conversions for ferroptosis–apoptosis combined anticancer therapy. *Acs Nano* **13**, 260–273 (2019).
32. Xue, C.-C. et al. Tumor microenvironment-activatable Fe-doxorubicin preloaded amorphous CaCO3 nanoformulation triggers ferroptosis in target tumor cells. *Sci. Adv.* **6**, eaax1346 (2020).
33. Klein, S. et al. Enhanced in vitro biocompatibility and water dispersibility of magnetite and cobalt ferrite nanoparticles employed as ROS formation enhancer in radiation cancer therapy. *Small* **14**, 1704111 (2018).
34. Zhou, Z. et al. Activatable singlet oxygen generation from lipid hydroperoxide nanoparticles for cancer therapy. *Angew. Chem.* **129**, 6592–6596 (2017).
35. Shen, Z. et al. Fenton-reaction-acceleratable magnetic nanoparticles for ferroptosis therapy of orthotopic brain tumors. *ACS Nano* **12**, 11355–11365 (2018).
36. Yue, L. et al. Development of a novel FePt-based multifunctional ferroptosis agent for high-efficiency anticancer therapy. *Nanoscale* **10**, 17858–17864 (2018).
37. Yao, X. et al. A novel multifunctional FePt/BP nanoplatform for synergistic photothermal/photodynamic/chemodynamic cancer therapies and photothermally-enhanced immunotherapy. *J. Mater. Chem. B* **8**, 8010–8021 (2020).
38. Meng, Y. et al. Core–shell FePt-cube@ covalent organic polymer nanocomposites: a multifunctional nanocatalytic agent for primary and metastatic tumor treatment. *J. Mater. Chem. B* **8**, 11021–11032 (2020).
39. Li, Z.-H., Chen, Y., Zeng, X. & Zhang, X.-Z. Ultra-small FePt/siRNA loaded mesoporous silica nanoplatform to deplete cysteine for enhanced ferroptosis in breast tumor therapy. *Nano Today* **38**, 101150 (2021).
40. Fromain, A., Perez, J., Van de Walle, A., Lalatonne, Y. & Wilhelm, C. Photothermia at the nanoscale induces ferroptosis via nanoparticle degradation. *Nat. Commun.* **14**, 4637 (2023).
41. He, S., Jiang, Y., Li, J. & Pu, K. Semiconducting polycomplex nanoparticles for photothermal ferrotherapy of cancer. *Angew. Chem. Int. Ed.* **59**, 10633–10638 (2020).
42. Zhu, T. et al. Ferroptosis promotes photodynamic therapy: supramolecular photosensitizer-inducer nanodrug for enhanced cancer treatment. *Theranostics* **9**, 3293 (2019).
43. Guan, Q. et al. Mesoporous polydopamine carrying sorafenib and SPIO nanoparticles for MRI-guided ferroptosis cancer therapy. *J. Control. Release* **320**, 392–403 (2020).
44. Gharibshahi, E. & Saion, E. Influence of dose on particle size and optical properties of colloidal platinum nanoparticles. *Int. J. Mol. Sci.* **13**, 14723–14741 (2012).
45. Bigall, N. C. et al. Monodisperse platinum nanospheres with adjustable diameters from 10 to 100 nm: synthesis and distinct optical properties. *Nano Lett.* **8**, 4588–4592 (2008).
46. Yu, J. et al. Synergistic enhancement of immunological responses triggered by hyperthermia sensitive Pt NPs via NIR laser to inhibit cancer relapse and metastasis. *Bioactive Mater.* **7**, 389–400 (2022).

47. Sangnier, A. P. et al. Raspberry-like small multicore gold nanostructures for efficient photothermal conversion in the first and second near-infrared windows. *Chem. Commun.* **55**, 4055–4058 (2019).

48. Oladipo, A. O., Nkambule, T. T., Mamba, B. B. & Msagati, T. A. Therapeutic nanodendrites: current applications and prospects. *Nanoscale Adv.* **2**, 5152–5165 (2020).

49. Potrč, T., Kralj, S., Nemec, S., Kocbek, P. & Kreft, M. E. The shape anisotropy of magnetic nanoparticles: an approach to cell-type selective and enhanced internalization. *Nanoscale* **15**, 8611–8618 (2023).

50. Mandriota, G. & Di Corato, R. Clustering of Magnetic Nanoparticles for Nanomedicine. *Magnetic Nanoparticles in Human Health and Medicine: Current Medical Applications and Alternative Therapy of Cancer*, 59–86 (Wiley, 2021).

51. Timoshenko, J. & Roldan Cuenya, B. In situ/operando electrocatalyst characterization by X-ray absorption spectroscopy. *Chem. Rev.* **121**, 882–961 (2020).

52. Chen, T.-Y. et al. Crystal shape controlled H2 storage rate in nanoporous carbon composite with ultra-fine Pt nanoparticle. *Sci. Rep.* **7**, 1–9 (2017).

53. Bernini, F. et al. Effective and selective trapping of volatile organic sulfur derivatives by montmorillonite intercalated with a μ-oxo Fe (III)–phenanthroline complex. *ACS Appl. Mater. Interfaces* **9**, 1045–1056 (2017).

54. Scarabelli, L., Sánchez-Iglesias, A., Pérez-Juste, J. & Liz-Marzán, L. M. "Tips and Tricks" Practical Guide to the Synthesis of Gold Nanorods. Vol. 6 4270–4279 (ACS Publications, 2015).

55. Hsieh, B.-J. et al. Platinum loaded on dual-doped TiO2 as an active and durable oxygen reduction reaction catalyst. *NPG Asia Mater.* **9**, e403–e403 (2017).

56. Van de Walle, A., Kolosnjaj-Tabi, J., Lalatonne, Y. & Wilhelm, C. Ever-evolving identity of magnetic nanoparticles within human cells: The interplay of endosomal confinement, degradation, storage, and neocrystallization. *Acc. Chem. Res.* **53**, 2212–2224 (2020).

57. Espinosa, A. et al. Intracellular biodegradation of Ag nanoparticles, storage in ferritin, and protection by a Au shell for enhanced photothermal therapy. *ACS Nano* **12**, 6523–6535 (2018).

58. Curcio, A. et al. Massive intracellular remodeling of CuS nanomaterials produces nontoxic bioengineered structures with preserved photothermal potential. *ACS Nano* **15**, 9782–9795 (2021).

59. Mazuel, F. et al. Magneto-thermal metrics can mirror the long-term intracellular fate of magneto-plasmonic nanohybrids and reveal the remarkable shielding effect of gold. *Adv. Funct. Mater.* **27**, 1605997 (2017).

60. Ayad, A. I. et al. Water soluble" palladium nanoparticle engineering for C–C coupling, reduction and cyclization catalysis. *Green Chem.* **21**, 6646–6657 (2019).

61. Plan Sangnier, A. et al. Endosomal confinement of gold nanospheres, nanorods, and nanoraspberries governs their photothermal identity and is beneficial for cancer cell therapy. *Adv. Biosyst.* **4**, 1900284 (2020).

62. Simonelli, L. et al. CLÆSS: The hard X-ray absorption beamline of the ALBA CELLS synchrotron. *Cogent Phys.* **3**, 1231987 (2016).

63. Ravel, B. & Newville, M. ATHENA, ARTEMIS, HEPHAESTUS: data analysis for X-ray absorption spectroscopy using IFEFFIT. *J. Synchrotron Radiat.* **12**, 537–541 (2005).

64. Newville, M. et al. Analysis of multiple-scattering XAFS data using theoretical standards. *Phys. B: Condens. Matter* **208**, 154–156 (1995).

Author contributions

E.G. and C.W. conceptualized the study. E.G. and Y.L. produced the nanoparticles. A.F. performed the heating experiments for aqueous dispersion and cellular suspensions, A.S. and A.E. performed XAS experiments, G.G. produced the microwells for spheroids formation, and C.W. performed high-throughput photothermal experiments on cancer spheroids in microwells. C.W. wrote the manuscript. E.G., A.S., Y.L., and A.E. proofread the manuscript.

Competing interests

The authors declare no competing interests.

Additional information

Supplementary information The online version contains supplementary material available at https://doi.org/10.1038/s43246-023-00411-1.

Correspondence and requests for materials should be addressed to Claire Wilhelm.

Peer review information *Communications Materials* thanks the anonymous reviewers for their contribution to the peer review of this work. Primary Handling Editor: Jet-Sing Lee. A peer review file is available.

Reprints and permission information is available at http://www.nature.com/reprints

Publisher's note Springer Nature remains neutral with regard to jurisdictional claims in published maps and institutional affiliations.